energies

MDPI

Article

In Situ Binder-Free and Hydrothermal Growth of Nanostructured $NiCo_2S_4$/Ni Electrodes for Solid-State Hybrid Supercapacitors

M. Mohamed Ismail [1], Zhong-Yun Hong [2], M. Arivanandhan [1], Thomas Chung-Kuang Yang [3], Guan-Ting Pan [3,*] and Chao-Ming Huang [2,*]

[1] Centre for Nanoscience and Technology, Anna University, Chennai 600025, India; mohamedismailnano@gmail.com (M.M.I.); arivucz@gmail.com (M.A.)
[2] Green Energy Technology Research Center and Department of Materials Engineering, Kun Shan University, Tainan 710, Taiwan; st112926@gmail.com
[3] Department of Chemical Engineering and Biotechnology, National Taipei University of Technology, Taipei 106, Taiwan; ckyang@mail.ntut.edu.tw
* Correspondence: gtpan@ntut.edu.tw (G.-T.P.); charming@ksu.edu.tw (C.-M.H.)

Abstract: Herein, we report a comparison of the electrochemical performance of two kinds of $NiCo_2S_4$-based electrodes for solid-state hybrid supercapacitors (HSCs). For the binder-free electrode, $NiCo_2S_4$ was grown on Ni foam by the chemical bath deposition (CBD) method. For the binder-using electrode, $NiCo_2S_4$ powder was synthesized by the hydrothermal method. FESEM images depicted the hierarchical nanostructure of $NiCo_2S_4$ synthesized by the hydrothermal method and uniform distribution of nanostructured $NiCo_2S_4$ grown on Ni foam by the CBD method. Half-cell studies of both $NiCo_2S_4$ electrodes showed them exhibiting battery-type charge storage behavior. To assemble HSCs, $NiCo_2S_4$ and activated carbon were used as a positive and negative electrode, respectively. Electrochemical studies of the HSCs showed that the accessible potential window was wide, up to 2.6 V, through cyclic voltammetry (CV) analysis. Chronopotentiometry (CP) studies revealed that the energy and power densities of binder-using HSC were 51.24 Wh/kg and 13 kW/kg at 1 Ag^{-1}, respectively, which were relatively higher than those of the binder-free HSC. The binder-free HSC showed 52% cyclic stability, relatively higher than that of the binder-using HSC. Both HSCs, with unique benefits and burdens on energy storage performance, are discussed in this work.

Keywords: $NiCo_2S_4$; binder-free electrode; chemical bath deposition; gel electrolyte; solid-state hybrid supercapacitor

Citation: Ismail, M.M.; Hong, Z.-Y.; Arivanandhan, M.; Yang, T.C.-K.; Pan, G.-T.; Huang, C.-M. In Situ Binder-Free and Hydrothermal Growth of Nanostructured $NiCo_2S_4$/Ni Electrodes for Solid-State Hybrid Supercapacitors. *Energies* **2021**, *14*, 7114. https://doi.org/10.3390/en14217114

Academic Editors: Worapon Kiatkittipong and Jun-Wei Lim

Received: 18 September 2021
Accepted: 25 October 2021
Published: 1 November 2021

1. Introduction

Supercapacitors store electrical energy in various unusual ways compared to conventional energy storage devices such as batteries and capacitors [1,2]. The storage behaviors of supercapacitors are classified as electrochemical double layer capacitance (EDLC) and pseudocapacitance. In these storage behaviors, electrical charge is stored in the electrode/electrolyte interface (EDLC—nonfaradaic reaction) and in surface or near-surface redox reactions at the electrode/electrolyte interface (pseudocapacitance—faradaic reaction). In recent years, some faradaic-dominated battery-type electrode materials have also been used as electrode materials in supercapacitors because of diffusion-controlled kinetics. Diverse ways to progress the storage capacity of symmetric and asymmetric supercapacitors have been discussed. Among these methods, hybrid supercapacitors (HSCs) represent a promising approach to achieve high energy density without lowering power density and maintain excellent cyclic stability operated in a wide potential window [3–7]. In HSCs, battery-type materials such as bimetallic oxides and lithiated metal oxide have been used as positive electrodes. On the other hand, EDLC-based materials such as activated carbon, CNT, and graphene and its derivatives have been used as negative electrode

materials [8–10]. The reason for using different types of electrode in the positive and negative side of HSCs is to widen the device's potential window, as widening the potential window increases the power and energy density [11]. Furthermore, battery-type materials enhance the storage capacity of the supercapacitor due to their faradaic-dominant charge storage behavior. However, numerous factors influence supercapacitor performance, such as contact resistance between the electrode and current collector, the uniformity of the electrode material coating on the current collector, the electrolyte decomposition point, and the oxidation point of the current collectors. To overcome these issues, specific materials and strategies need to be implemented.

The selection of electrode materials plays a crucial role in the performance of the HSCs. Spinel-structured materials such as $ZnCo_2O_4$, $CoFe_2O_4$, $LiMn_2O_4$, $NiCo_2O_4$, and $CuCo_2S_4$ are superior battery-type electrode materials for supercapacitor application [12–17]. Among those materials, $NiCo_2S_4$ is a profound thiospinel electrode material with high electrical conductivity, low optical band gap, and favorable electron transport structure compared to its monometal sulfide and oxide spinel $NiCo_2O_4$ counterparts [18–23]. In many reports, $NiCo_2S_4$ was synthesized by hydrothermal, solvothermal, and coprecipitation methods [24–28]. From these methods, the $NiCo_2S_4$ powders were coated on the current collector using a low-conductivity binder. This binder might influence the electrical conductivity of the electrode material and hinder the electron transport between the current collector and electrode material. To avoid that, $NiCo_2S_4$ was grown on Ni foam by the binder-free CBD method followed by calcination under an inert atmosphere in the present work. CBD is a novel method to directly grow electrode material on the current collector. The CBD method had some unique benefits compared to the conventional coating method, such as lowering the charge transfer resistance between the current collector and electrode material, uniform growth of electrode material, ease of controlling the growth of electrode material, and favoring mass production of electrode material with its homogeneous growth [29].

In addition to the selection of electrode material and synthesis method, the electrolyte and current collector also play critical roles in the performance of HSCs. There are various types of electrolytes used in HSC applications. Aqueous, nonaqueous, solid- state, inorganic, dry solid polymer, and redox-active gel polymer electrolyte have all been employed in HSC development. From the above electrolyte types, carboxymethyl cellulose and KOH (CMC/KOH)-based gel electrolyte show high accessible potential windows, amended attachment with electrode material, nontoxicity, high dielectric constants, and high thermal and chemical stability [30–35]. Furthermore, various kinds of current collectors have used in the development of HSCs, including Ni foam, Al foil, carbon cloth, Ni foil, and stainless-steel mesh. The current collector should have a high oxidation point and high electrochemical stability [36–38]. In this present work, carbon-coated Ni foam was used as a current collector and CMC/KOH gel as an electrolyte to widen the potential window of the HSCs.

To investigate the intrinsic properties of $NiCo_2S_4$ for utilization as a supercapacitor electrode, two kinds of $NiCo_2S_4$ electrodes were prepared. The first was a nanostructured $NiCo_2S_4$ film was grown directly on the current collector by the CBD method, which served as the binder-free electrode. The other was a $NiCo_2S_4$ powder synthesized by the hydrothermal (HT) method, which was coated on the current collector with PVDF binder without any conductive additives and which served as the binder-using electrode. In many research works, aqueous or polymer gel-based electrolytes have been used; however, works employing cellulose-based gel electrolytes were very few. Comparative analyses of electrode coating methods using the same material were also limited in the previous literature. This type of work helps to understand the influence of the engineering and configuration of a device over the chemistry and structure of the electrode material.

2. Materials and Methods

2.1. Material Details

The reagents nickel acetate, cobalt acetate, thioacetamide, and PVDF were purchased as analytical grade without any additional purification from PanReac Applichem (Spain). Ni foam was purchased from ChangSha Lyrun New Material Co. Ltd., Changsha, China, 110 pores per square inch.

2.2. Hydrothermal Synthesis of $NiCo_2S_4$ Powder and Binder-Using Electrode Preparation

The $NiCo_2S_4$ powder was prepared as follows. First, 0.1 M nickel acetate, 0.2 M cobalt acetate, and 0.4 M thioacetamide were dissolved in 160 mL of deionized (DI) water and stirred for 15 min. Then, the solution was transferred into a 200 mL Teflon-lined stainless-steel autoclave and kept in a box furnace for 6 h at 200 °C. Finally, the collected product was washed with DI water and ethanol mixture several times and dried in a vacuum oven for 12 h at 100 °C. For the preparation of the binder-using electrode, $NiCo_2S_4$ powders and polyvinylidene fluoride (PVDF) binder were mixed with 400 µL N-Methyl-2-Pyrrolidone (NMP) in mortar and pestle to make an ink-like slurry. To make a comparison of the intrinsic properties of NCS, conductive additives were not used. Then, the electrode was coated on 2 cm × 3 cm Ni foam and dried in a vacuum oven for 6 h at 70 °C. In this article, NCS(PW)/Ni refers to hydrothermally synthesized $NiCo_2S_4$ powder coated on Ni foam using a PVDF binder. This same notation refers to the hybrid supercapacitor assembled with the aforementioned $NiCo_2S_4$ electrode. Figure 1 schematically represents the synthesis process of $NiCo_2S_4$ by the hydrothermal method.

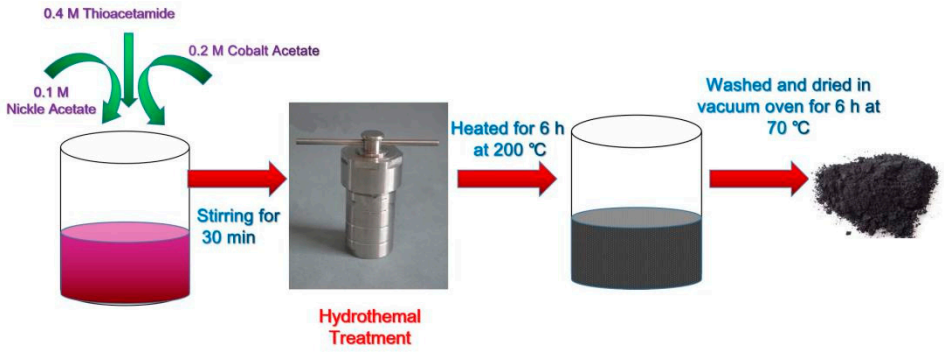

Figure 1. The synthesis process of $NiCo_2S_4$ by the hydrothermal method.

2.3. Chemical Bath Deposition (CBD) of $NiCo_2S_4$ on Ni Foam as Binder-Free Electrode

For the preparation of binder-free electrode, 0.1 M nickel acetate, 0.2 M cobalt acetate, and 0.4 M thiourea were dissolved into 50 mL of DI water and stirred for 5 min; the solution turned pink throughout this process. Then, the solution was kept in a 90 °C preheated water bath and stirred at 400 rpm. In the above solution condition, 2 cm × 3 cm Ni foam was inserted and incubated for 45 min. After that, the Ni foam was removed, dried in a vacuum oven for 6 h, and then calcinated in a tubular furnace at 350 °C for 3 h in 100 cm/Hg N_2 flow. Finally, the Ni foam's weight was measured, and the difference in weight before and after the CBD process was considered as the $NiCo_2S_4$ electrode's mass. This process is schematically represented in Figure 2. In this article, NCS(CBD)/Ni referred to the electrode created through in situ growth of $NiCo_2S_4$ by the CBD method without using any binders. In half-cell and hybrid supercapacitor electrochemical analysis graphs, the same notation is used for the supercapacitors assembled with the same electrode.

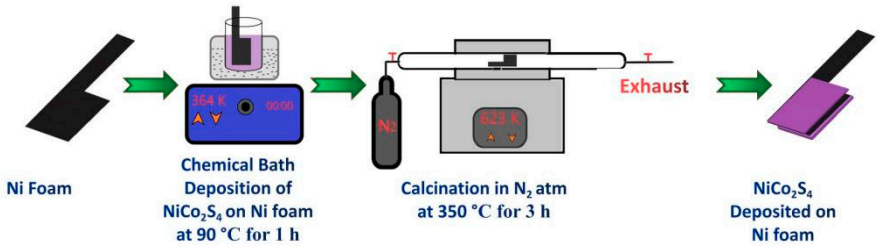

Figure 2. The chemical bath deposition process.

2.4. Electrochemical Measurements

Half-cell electrochemical measurements of $NiCo_2S_4$/Ni electrodes (NCS(PW)/Ni and NCS(CBD)/Ni) and activated carbon/Ni electrodes were performed in a 6 M KOH electrolyte. For the half-cell measurement, active electrode material/Ni foam was used as the working electrode, saturated calomel electrode (SCE) as the reference electrode, and platinum wire as the counter electrode. Cyclic voltammetry (CV) analyses were recorded from 100 to 5 mVs^{-1}. Chronopotentiometry (CP) analyses were recorded from 10 to 1. Electrochemical impedance spectroscopy (EIS) analyses were recorded at the AC frequencies in the 10 kHz to 0.1 Hz range.

2.5. Assembly of Hybrid Supercapacitor

Hybrid supercapacitors (HSCs) were assembled in the ambient condition using NCS(PW)/Ni or NCS(CBD)/Ni) as a positive electrode, activated carbon as a negative electrode, polypropylene sheet as a separator, (CMC)/KOH gel as a gel electrolyte, and antistatic aluminum film as an outer case. In the typical process, 2 g of CMC and 2 g of KOH were dissolved in 50 mL of DI water and then stirred at 45 °C for 20 h to make a gel. During stirring, the solvent was evaporated, and ~25 mL viscous CMC/KOH gel was obtained. After the assembling of the positive/negative electrodes and separator, CMC/KOH gel electrolyte was filled in between the positive and negative electrodes, and then the aluminum outer case was vacuum sealed.

2.6. Characterization Techniques

X-ray diffraction (PANalyticalX'Pert PRO, Almelo, The Netherlands) was performed with Cu radiation (λ = 0.15418 nm) in the 2θ range of 20–80°. The surface morphology of the prepared samples was captured by field emission scanning electron microscopy (JEOL JSM-6700F, Tokyo, Japan). The electrochemical measurements were analyzed using a CHI 6273E electrochemical workstation (CH Instruments, Inc. Austin, TX, USA).

2.7. Electrochemical Characterization

The specific capacity C_{sc} (Cg^{-1}) of the half cell and those of the HSCs from CV and CP measurement were calculated by following Equations (1) and (2), respectively:

$$C_{sc} = \frac{1}{mV_s} \int_{V_1}^{V_2} I(V) \quad (1)$$

where m is the mass loading (g) on the carbon-coated Ni foam electrode, Vs is the applied scan rate (mVs^{-1}), and I is the current (A) obtained from the applied scan rate;

$$C_{sc} = \frac{I\,dt}{m} \quad (2)$$

where I is the current density (Ag^{-1}) and dt is the discharge time (s). The energy and power density of the HSC were calculated by Equations (3) and (4), respectively:

$$E = 0.5C_{sc}V^2 \left(\text{Wh.kg}^{-1}\right) \quad (3)$$

$$P = E/t \left(\text{W.kg}^{-1}\right) \quad (4)$$

The mass balancing of the prepared positive and negative electrodes to assemble the HSC was calculated by Equation (5).

$$\frac{m_+}{m_-} = \frac{C_-\Delta V_-}{C_+\Delta V_+} \quad (5)$$

where m_+ and m_- were the active material mass loading (mg) on the positive and negative electrodes, respectively; C_+ and C_- were the specific capacities (F/g) of the positive and negative electrodes, respectively; and ΔV_+ and ΔV_- were the potential window (V) of the positive and negative electrodes, respectively. The proper mass balancing was effective to achieve high-performance HSCs [39]. The loaded masses of NCS(PW) and NCS (CBD) were ~2.4 mg/cm^{-1}.

3. Results and Discussion

3.1. Structural and Morphological Analysis of $NiCo_2S_4$

Figure 3a,b shows the XRD analysis results for $NiCo_2S_4$ prepared by the hydrothermal and CBD method, respectively. Both diffraction patterns coincided with Joint Committee on Powder Diffraction Standards (JCPDS) card no. 20–0782 [40–43]. Intense and broad peaks confirmed the formation of nanostructured $NiCo_2S_4$ created by the hydrothermal method (Figure 3a). On the other hand, the CBD-synthesized $NiCo_2S_4$ was directly deposited on the carbon-coated Ni foam, so the intensity of the Ni foam was dominant in the diffraction pattern. However, in the closed view, the peaks were matched with standard JCPDS data. From the XRD analysis, the thiospinel structure (AB_2S_4, where A and B are the M^{2+} and M^{3+} oxidation states, respectively) of $NiCo_2S_4$ was confirmed. In this thiospinel structure, Ni^{2+} occupied the tetrahedral site and Co^{3+} occupied the octahedral site with a built-in, tightly packed with the array of S^{-2} ions [44].

Figure 3c,d shows the Raman spectroscopic analysis results. The F_{2g} and A_{1g} modes of vibration were shown at 520 cm^{-1} and 661 cm^{-1}, respectively. This confirmed the formation of $NiCo_2S_4$ synthesized through the hydrothermal and CBD methods. In particular, CBD-synthesized $NiCo_2S_4$ was directly deposited on the carbon-coated Ni foam, so the G band vibration appeared at 1580 cm^{-1} [26–28].

Figure 3e,f depicts field emission scanning electron microscope (FESEM) images of $NiCo_2S_4$ synthesized from hydrothermal and CBD methods, respectively. The hydrothermal-synthesized $NiCo_2S_4$ showed a hierarchical nanostructure morphology. CBD-synthesized $NiCo_2S_4$ showed a relatively small nanostructure morphology compared to that of the hydrothermal method. Moreover, $NiCo_2S_4$ (CBD) showed better attachment with the Ni foam than its counterpart due to the direct in situ growth mechanism.

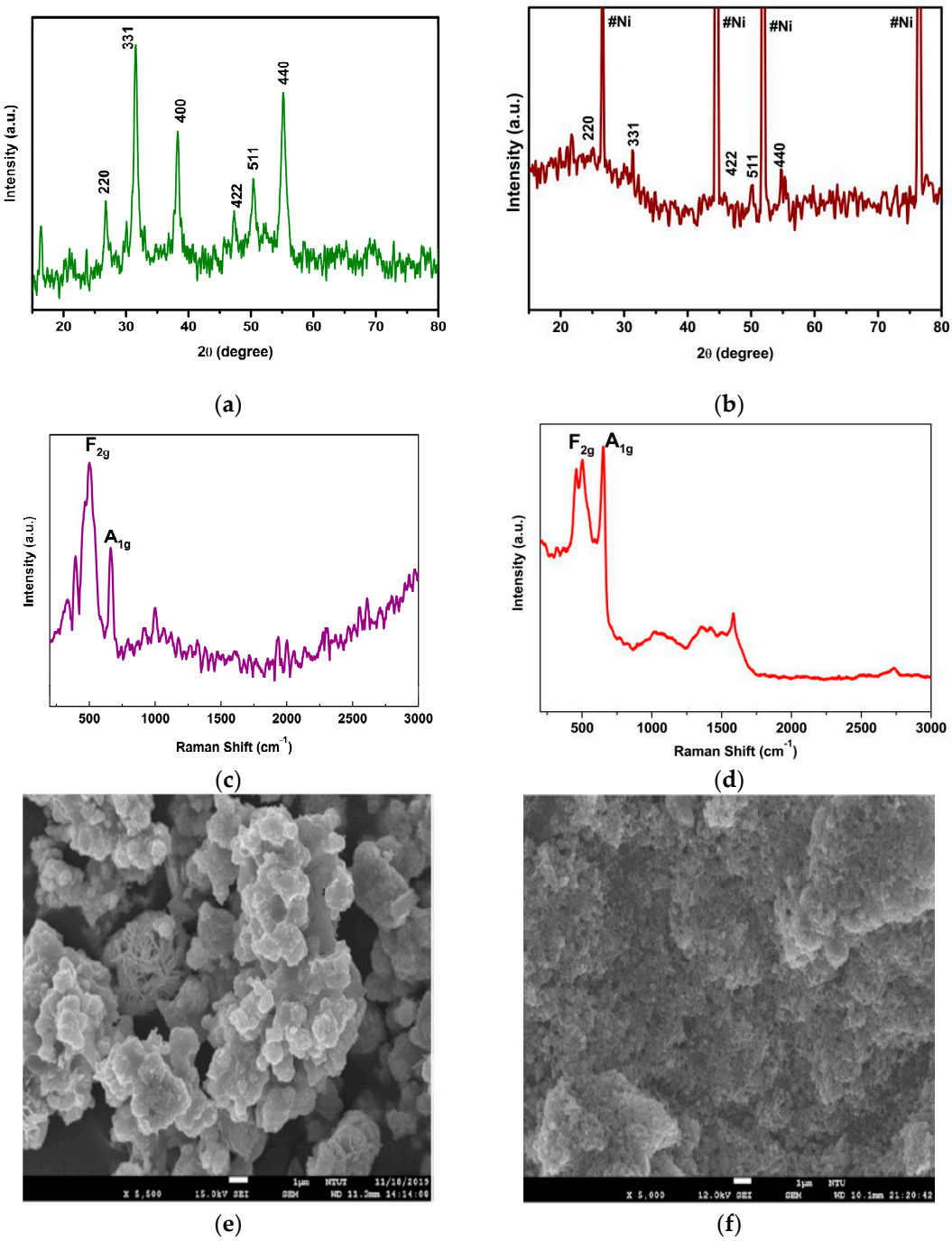

Figure 3. Structural and morphological analysis of $NiCo_2S_4$: (**a**) X-ray diffraction analysis of $NiCo_2S_4$ synthesized by the hydrothermal method, (**b**) X-ray diffraction analysis of $NiCo_2S_4$ synthesized by the CBD method; (**c**,**d**) Raman spectroscopic analysis of $NiCo_2S_4$ synthesized by the hydrothermal and CBD methods, respectively; (**e**,**f**) FESEM images of $NiCo_2S_4$ synthesized by the hydrothermal and CBD methods, respectively.

3.2. Electrochemical Performance of $NiCo_2S_4$ Materials

The electrochemical behavior of the synthesized $NiCo_2S_4$ was analyzed by a three-electrode setup. CV, CP, and EIS analysis results are shown in Figure 4. Figure 4a,d shows the CV curves of $NiCo_2S_4$ electrodes synthesized by the hydrothermal (NCS(PW)/Ni) and CBD methods (NCS(CBD)/Ni), respectively, with various sweep rates from 100 to 5 mVs^{-1}. The shapes of the CV curves were similar in both $NiCo_2S_4$ electrodes, and the NCS(PW)/Ni electrode showed higher current density than NCS(CBD)/Ni electrode. In terms of potential window, the NCS(CBD)/Ni electrode showed a 0.3 V wider potential

window (−0.1 to 0.6 V) than the NCS(PW)/Ni electrode (−0.1 to 0.3 V). In Figure 4a,d, the oxidation and reduction peaks present in the CV curves show the battery-type storage behavior of $NiCo_2S_4$ electrodes [44]. The higher current density and shorter potential window showed that the NCS(PW)/Ni electrode stored a greater amount of charge than the NCS(CBD)/Ni electrode, which resembles in the specific capacity of the electrode from Figure 4f. The specific capacity of the NCS(PW)/Ni electrode was relatively higher than that of NCS(CBD)/Ni electrode.

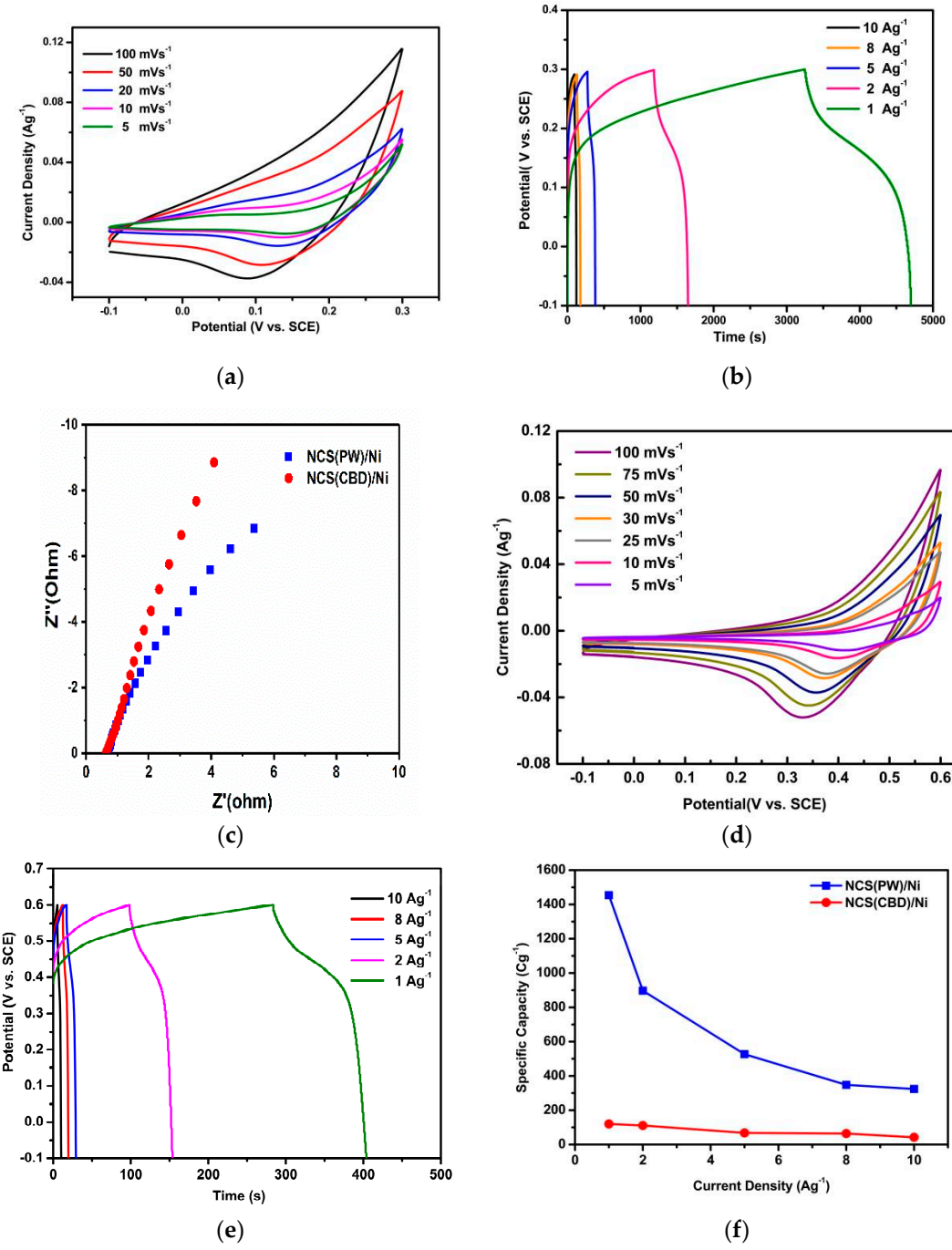

Figure 4. Electrochemical properties of $NiCo_2S_4$ materials: (**a**) the CV curves of $NiCo_2S_4$ electrodes synthesized by the hydrothermal method (NCS(PW)/Ni electrodes); (**b**) charging and discharging analysis by chronopotentiometry (CP) measurements for NCS(PW)/Ni electrodes; (**c**) the EIS spectra of both NCS(PW)/Ni and NCS(CBD)/Ni electrodes; (**d**) the CV curves of NCS(CBD)/Ni electrodes, (**e**) CP measurements of NCS(CBD)/Ni electrodes, (**f**) a comparison of the specific capacities of both NCS(PW)/Ni and NCS(CBD)/Ni electrodes.

Figure 4b,e shows the charging and discharging analysis by chronopotentiometry (CP) measurements of NCS(PW)/Ni and NCS(CBD)/Ni electrodes, respectively. The CP curves were recorded from 10 to 1 Ag^{-1} current rates. Both NCS(PW)/Ni and NCS(CBD)/Ni electrodes showed similar curve shapes. Moreover, the electrodes were able to charge at high to low current rates (10 to 1 Ag^{-1}); this indicated the superior capacitance behavior of the material. The iR drop of the NCS(PW)/Ni electrode was higher than that of the NCS(CBD)/Ni electrode because of the higher charge transfer resistance to release the stored charge from the NCS(PW)/Ni electrode, which was due to the lower-conductivity binder (Figure 4b,e). Furthermore, the electrode/electrolyte interface and resistance play major roles in the performance of the electrode. An electrode with a high electrode/electrolyte interface and lower interface resistance stores more energy than a highly resistive electrode [37,38,45]. Apart from the iR drop analysis from CP curves, the resistance and charge storage behavior of the electrode material can be analyzed by EIS measurements. Figure 4c shows the EIS spectra of both NCS(PW)/Ni and NCS(CBD)/Ni electrodes. The initial starting point of the curve was considered as the bulk electrolyte resistance or electrochemical series resistance (ESR). These resistances were responsible for contact resistance between the electrode material and the current collector [46–50]. NCS(CBD)/Ni electrode showed a 0.6 Ω ESR which is relatively lesser than the NCS(PW)/Ni electrode's 1.8 Ω ESR value, which confirms the in situ binder-free growth CBD process reduced the contact resistance between the current collector and electrode material [51–53].

Figure 4f shows a comparison of the specific capacities (Cg^{-1}) of both NCS(PW)/Ni and NCS(CBD)/Ni electrodes. The results showed 1454.3 $Cg^{-1}$and 120.6 Cg^{-1} specific capacities for NCS(PW)/Ni and NCS(CBD)/Ni electrodes, respectively, at a 1 Ag^{-1} current density. The specific capacity of NCS(PW)/Ni was perceptibly higher than that of NCS(CBD)/Ni at all sweep rates. With the specific capacity values of the positive and negative electrodes (activated carbon/Ni foam), the loading mass (g) of the active materials on the Ni foam was balanced using Equation (5).

3.3. Electrochemical Measurements of $NiCo_2S_4$/Activated Carbon Hybrid Supercapacitors

The negative electrode (activated carbon) showed a potential window in the 0 to −1 V range. In the aqueous electrolyte, the total potential window of the cells was 1.5 V and 1.6 V for NCS(PW)/Ni and NCS(CBD)/Ni electrodes, as shown in Figure 5a,c. Figure 5b,d shows the CV of NCS(PW)/Ni and NCS(CBD)/Ni HSCs, respectively, from 2 to 3 V of the potential window in the CMC/KOH gel electrolyte. The curves were similar and extended the potential window up to 2.8 V for the NCS(PW)/Ni HSC (recorded from −1.4 to 1.4 V), and 3 V for the NCS(CBD)/Ni HSC (−1.5 to 1.5 V). In the CV curves of the HSCs, positive potential oxidation and reduction peaks due to Ni and Co ions appeared. The increase in the cell voltage was due to the usage of cellulose-based gel electrolytes. In the gel-based electrolyte, the solvent was evaporated during the gel preparation process, so electrolyte decomposition due to water was prevented. In the CMC/KOH gel electrolyte, solvated ions were surrounded by a complex CMC matrix; that matrix enhanced the electrode/electrolyte interactions through strong attachment of the electrolyte to the electrode material [33–35]. Moreover, the current collector was coated with a thin layer of carbon, so the oxidation of the Ni current collector was inhibited. The carbon coating also gave electrochemical stability during a wider potential window [36].

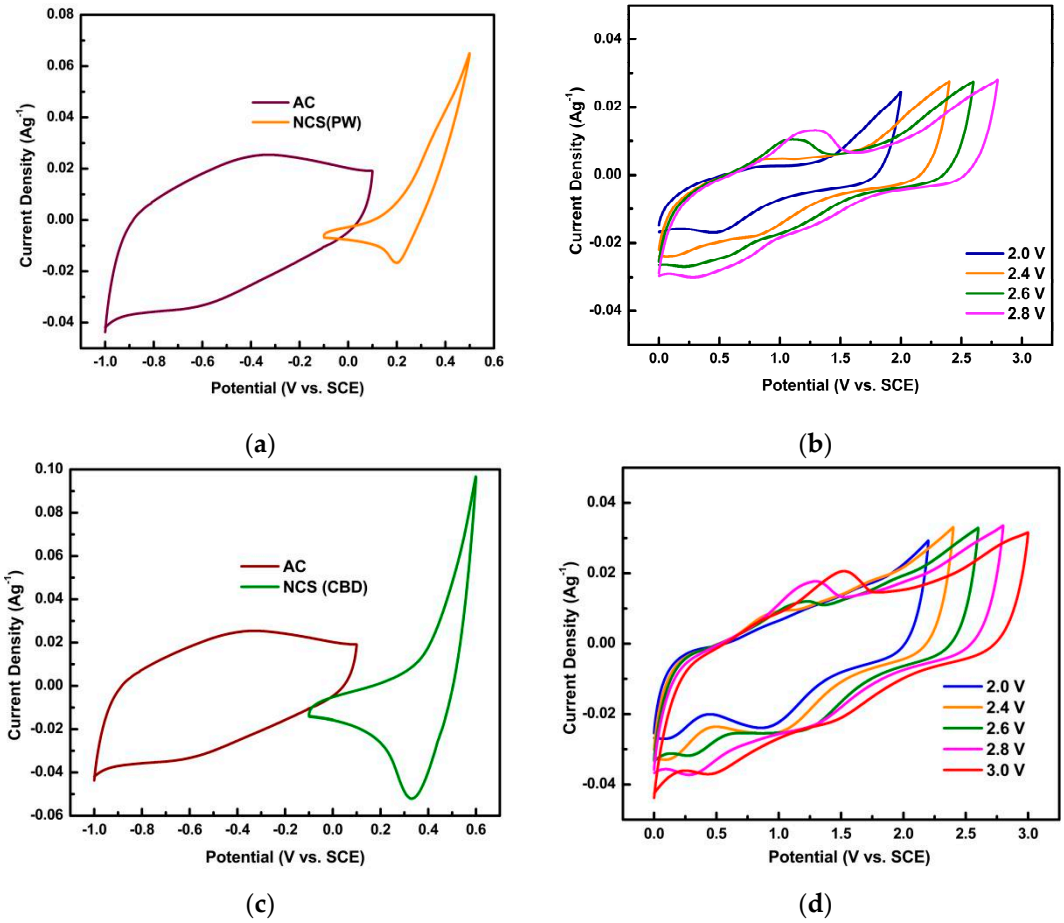

Figure 5. Electrochemical properties of $NiCo_2S_4$/activated carbon hybrid supercapacitors: (**a**) the total potential window of 1.5 V for NCS(PW)/Ni electrodes; (**b**) the CV of the NCS(PW)/Ni HSC; (**c**) the total potential window of 1.6 V for NCS(CBD)/Ni electrodes; (**d**) the CV of the NCS(CBD)/Ni HSC.

Figure 6a,b shows the results of CP analysis of NCS(CBD)/Ni and NCS(PW)/Ni HSCs, respectively, with scan rates from 1 to 10 Ag^{-1}. The charging and discharging curves reached up to 2.6 V for both NCS (PW)/Ni and NCS(CBD)/Ni HSCs at all scan rates. This CP curves exploits that assembled HSCs were profound design to develop high voltage HSC. The NCS(PW)/Ni HSC showed a longer discharge time than the NCS(CBD)/Ni HSC as well as a higher potential window. As shown in Figure 6a,b, the NCS(PW)/Ni HSC had a high iR drop at initial discharge time compared to that of NCS(CBD)/Ni HSC. The iR drop was rapid discharge at a high potential rate; this kind of sudden discharge was due to the high ESR value of the HSC components. From EIS analysis, the NCS(CBD)/Ni electrode had a lower ESR value. The high impedance in the NCS(PW)/Ni HSC caused a huge iR drop in the CP curves. Even with this iR drop, the discharge time was prolonged and the potential window was wider, leading to higher power and energy density for the HSC [39]. Figure 6c shows the comparative specific capacities of NCS(PW)/Ni and NCS(CBD)/Ni HSCs. The NCS(PW)/Ni HSC delivered a higher specific capacity than the NCS(CBD)/Ni HSC. Figure 6d depicts the EIS curve of the assembled HSCs. The ESR value of the binder-free electrode (2.5 Ω) was much lower than that of the binder-using electrode (4.8 Ω). The assembled HSCs' ESR values were higher than those of the half-cell electrodes because the HSCs had electrolyte and negative electrode resistance, which were added to the total ESR of the HSCs [54–56]. Figure 6e shows a Ragone plot of energy vs. power density for NCS(PW)/Ni and NCS(CBD)/Ni HSCs compared to the literature mentioned in Table 1. The power and energy densities of the NCS(CBD)/Ni HSC were 13 kW/kg and

29.11 Wh/kg, respectively, which were relatively lower than those of the NCS(PW)/Ni HSC with power density of 13 kW/kg and energy density of 51.24 Wh/kg at 1 Ag^{-1}.

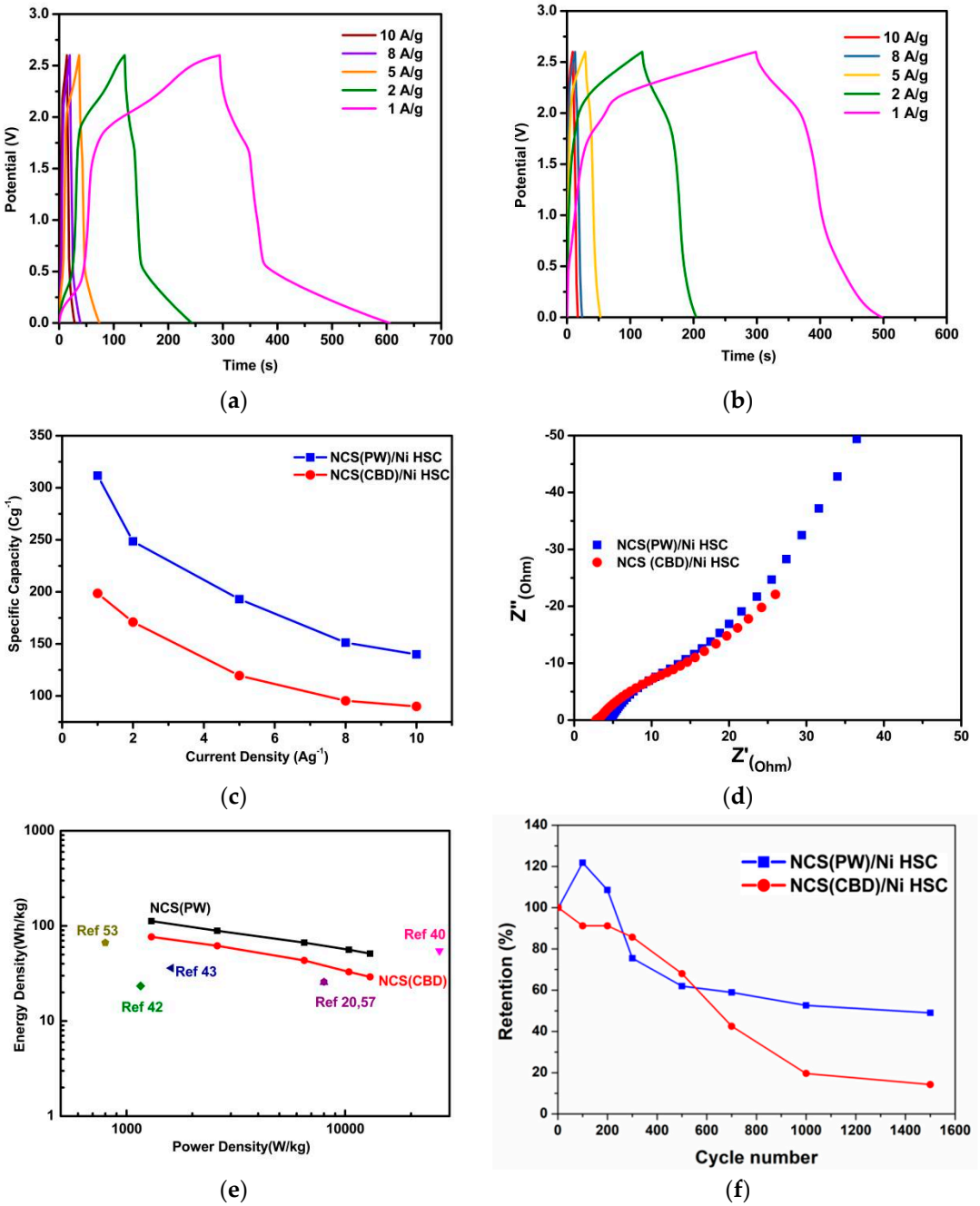

Figure 6. Electrochemical evaluation of NCS(CBD)/Ni and NCS(PW)/Ni HSCs: (**a**) CP analysis of the NCS(CBD)/Ni HSC; (**b**) CP analysis of the NCS(PW)/Ni HSC; (**c**) the comparative specific capacities of NCS(PW)/Ni and NCS(CBD)/Ni HSCs, (**d**) the EIS curves of the assembled HSCs, (**e**) Ragone plot of energy vs. power density for NCS(PW)/Ni and NCS(CBD)/Ni HSCs; (**f**) cyclic stability results of NCS(CBD)/Ni and NCS(PW)/Ni HSCs analyzed for 1500 cycles.

Table 1. Comparisons of the present work with previously reported $NiCo_2S_4$-based supercapacitors.

Material and Substrate	Synthesis Method	Morphology	Potential Window Full Cell	Specific Capacitance or Capacity	Energy Density	Power Density	Cyclic Stability	Ref.
$NiCo_2S_4$-Ni foam	Hydrothermal	Mesoporous nanosheet	1.6 V	744 Fg^{-1} @ 1 Ag^{-1}	25.5 Wh/kg	8 kW/kg	93.4% 1500 cycles	[20]
$NiCo_2S_4$/polyaniline-Carbon Cloth	Hydrothermal/ chemical oxidative polymerization	Petal-like nanosheet	1.6 V	1879 Fg^{-1} @ 1 Ag^{-1}	54.6 Wh/kg	27.1 W/kg	72%	[41]
$NiCo_2S_4$-Ni foam	Hydrothermal	Hydrangea flower	—	1475 Fg^{-1} @ 3 Ag^{-1}			78.1%	[42]
$NiCo_2S_4$/graphene hydrogel−Ni foam	Hydrothermal	Nanosphere	1.6 V	23 mAg^{-1} @1 Ag^{-1}	23.38 Wh/kg	1.16 kW/kg	91.4% 5000 cycles	[43]
$NiCo_2S_4$/rGO−Ni foam	Hydrothermal	Hierarchic porous	1.5 V	1107 Fg^{-1} @ 1 Ag^{-1}	36 Wh/kg	1.6 kW/kg	85% 8000 cycles	[44]
Hollow mesoporous $NiCo_2S_4$−Ni foam	Hydrothermal	Ellipsoids	1.5 V	607 Fg^{-1} @ 3 Ag^{-1}	28.9 Wh/kg	187.5 W/kg	71.9% 2500 cycles	[53]
$NiCo_2S_4$	Hydrothermal	Nanosheets	1.7	844 Cg^{-1} @ 1 Ag^{-1}	25.8 Wh/kg	8kW/kg	72.5%	[57]
$NiCo_2S_4$@$Co(OH)_2$−Ni foam	In situ hydrothermal growth	Core–shell nanotube array	1.6 V	9.6 F/cm^2 @ 2 mA/cm^2	35.89 Wh/kg	0.4 kW/kg	70.1%	[58]
$NiCo_2S_4$@$CoMoO_4$ (core−shell)−carbon cloth	Hydrothermal	Core–shell nanowire arrays	1.6 V	2118.8 Fg^{-1} @ 1 Ag^{-1}	66.6 Wh/Kg	0.8 kW/Kg	85.6% 5000 cycles	[59]
NCS(PW)/Ni/AC	Hydrothermal	Nanohierarchical structure	2.6 V	311.7 Cg^{-1} @ 1 Ag^{-1}	51.24 Wh/Kg	13 kW/kg	14% 1500 cycles	This work
NCS(CBD)/Ni/AC	Chemical bath deposition	Spherical morphology	2.6 V	198.6 Cg^{-1} @ 1 Ag^{-1}	29.1 Wh/Kg	13 kW/kg	52% 1500 cycles	This work

Cyclic stability analysis gives insight about the charge storage capability of the supercapacitor for prolonged cycles. Figure 6f shows the cyclic stability results of NCS(CBD)/Ni and NCS(PW)/Ni HSCs for 1500 cycles. The cyclic stability of NCS(CBD)/Ni and NCS(PW)/Ni HSCs was 52% and 14%, respectively. The effect of the binder and high impedance in NCS(PW)/Ni HSC components reduced the stability of the HSC even with high energy and power density. On the other hand, the binder-free NCS(CBD)/Ni HSC, with less impedance in the HSC component and stable coating on the Ni foam, had relatively higher stability compared to the NCS(PW)/Ni HSC. Moreover, the binder-free HSC showed >20% cyclic retention in the initial 200 cycles due to the formation of a new ion=diffusion path in the electrode structure, which is called the "activation process". After that, the stability was retained up to 52%. After the same initial 200 cycles, the NCS(PW)/Ni HSC showed better stability due to the hierarchical structure of $NiCo_2S_4$, but the absence of conductive additives and the resistive binder reduced the stability after 200 cycles compared to the NCS(CBD)/Ni HSC. Moreover, from the CP curves, the iR drop was less in the NCS(CBD)/Ni HSC, which improved its stability because of its structural stability and lower-impedance HSC components. However, the cyclic stability was relatively lower compared to previously reported HSCs with similar types of materials that were mentioned in Table 1. In Table 1, the reported HSCs' working potential window was restricted to a maximum of 1.7 V; above 2 V, the reports are scarce because of the degradation of electrode and decomposition of electrolyte. However, because of this, all solid-state HSCs with polymer/cellulose gel-based electrolyte structure gave up access to a 2.6 V potential window as well as high energy and power density with reasonable cyclic stability. The weak stability of the material was due to the battery-type energy storage behavior of the material. The performance of battery-behavior materials could be limited by the diffusion of reactant molecules or ions, phase transformation, and chemical binding changes. A possible solution to improve the stability of the binder-free HSC is to composite the electrode material with high-surface graphitic carbons as nanocomposites [57–62].

4. Conclusions

$NiCo_2S_4$ electrodes were synthesized by the chemical bath deposition and hydrothermal methods. Structural and morphological analysis such as XRD and FESEM showed the

crystal structure and nanohierarchical morphology of the synthesized $NiCo_2S_4$ electrodes. Raman spectra confirmed the formation of spinel−structure $NiCo_2S_4$ through the A_{1g} and E_{2g} modes of vibration present at 520 cm^{-1} and 661 cm^{-1}, respectively. As seen from electrochemical analysis, both binder−free and binder−using HSC had added benefits and drawbacks. Cyclic voltammetry analysis showed that both HSCs were stable up to 2.6 V without any electrolyte decomposition. Chronopotentiometry analysis revealed that the binder−using HSC had a huge iR drop compared to the binder−free HSC. The resistance at the electrode/electrolyte interface was relatively higher for the binder−using HSC compared to the binder−free HSC. These resistances directly affected the stability of the supercapacitor. In terms of energy storage performance, the specific capacity (Cg^{-1}) of the binder−using HSC (311.7 Cg^{-1}) was higher than that of the binder−free HSC (198.6 Cg^{-1}) at 1 Ag^{-1} current density. Moreover, the power density was equal for both HSCs. However, the binder−free HSC showed higher performance in cyclic stability (52%) and lower energy density (29.11 Wh/kg) compared to the binder−using HSC (51.24 Wh/kg). As a comparative analysis, the binder−free HSC has added advantages over the binder−using HSC because of the easy uniform coating of electrode materials. The CMC/KOH electrolyte showed profound energy storage performance in both HSCs. Finally, the battery−type electrode material, gel electrolyte, and optimized coating methods conjointly enhanced the storage capacity and performance of the supercapacitor.

Author Contributions: Writing—original draft preparation, M.M.I.; formal analysis and data curation, Z.-Y.H.; investigation, M.A.; resources, T.C.-K.Y.; formal analysis and writing—review and editing, G.-T.P.; writing—review and editing, supervision, and funding acquisition, C.-M.H. All authors have read and agreed to the published version of the manuscript.

Funding: This work was financially supported by the Green Energy Technology Research Center from the Featured Areas Research Center Program within the framework of the Higher Education Sprout Project and TEEP@AsiaPlus by the Ministry of Education (MOE) in Taiwan. Author M. Mohamed Ismail is thankful to the Ministry of Education (MOE) in Taiwan and Kun Shan University to accomplish this work through the TEEP@AsiaPlus program and to Anna University for the Anna Centenary Research Fellowship (CRF/ACRF/2018/AR1/50).

Institutional Review Board Statement: Not applicable.

Informed Consent Statement: Not applicable.

Data Availability Statement: Not applicable.

Conflicts of Interest: The authors declare that they have no conflicts of interest.

References

1. Xie, J.; Yang, P.; Wang, Y.; Qi, T.; Lei, Y.; Li, C.M. Puzzles and confusions in supercapacitor and battery: Theory and solutions. *J. Power Sources* **2018**, *401*, 213–223. [CrossRef]
2. Chen, G.Z. Supercapacitor and supercapattery as emerging electrochemical energy stores. *Int. Mater. Rev.* **2017**, *62*, 173–202. [CrossRef]
3. Okhay, O.; Tkach, A. Graphene/Reduced Graphene Oxide-Carbon Nano tubes Composite Electrodes: From Capacitive to Battery-Type Behaviour. *Nanomaterials* **2021**, *11*, 1240. [CrossRef] [PubMed]
4. Gogotsi, Y.; Penner, R.M. Energy storage in nanomaterials–capacitive, pseudocapacitive, or battery-like? *ACS Nano* **2018**, *12*, 2081–2083. Available online: https://pubs.acs.org/doi/full/10.1021/acsnano.8b01914 (accessed on 15 October 2021). [CrossRef]
5. Zuo, W.; Li, R.; Zhou, C.; Li, Y.; Xia, J.; Liu, J. Battery-supercapacitor hybrid devices: Recent progress and future prospects. *Adv. Sci.* **2017**, *4*, 1600539. [CrossRef]
6. Shao, Y.; El−Kady, M.F.; Sun, J.; Li, Y.; Zhang, Q.; Zhu, M.; Wang, H.; Dunn, B.; Kaner, R.B. Design and mechanisms of hybrid supercapacitors. *Chem. Rev.* **2018**, *118*, 9233–9280. [CrossRef] [PubMed]
7. Choudhary, N.; Li, C.; Moore, J.; Nagaiah, N.; Zhai, L.; Jung, Y.; Thomas, J. hybrid supercapacitor electrodes and devices. *Adv. Mater.* **2017**, *29*, 1605336. [CrossRef]
8. González, A.; Goikolea, E.; Barrena, J.A.; Mysyk, R. Review on supercapacitors: Technologies and materials. *Renew. Sustain. Energy Rev.* **2016**, *58*, 1189–1206. [CrossRef]
9. Augustyn, V.; Simon, P.; Dunn, B. Pseudocapacitive oxide materials for high−rate electrochemical energy storage. *Energy Environ. Sci.* **2014**, *7*, 1597–1614. [CrossRef]

10. Choi, C.; Ashby, D.S.; Butts, D.M.; DeBlock, R.H.; Wei, Q.; Lau, J.; Dunn, B. Achieving high energy density and high power density with pseudocapacitive materials. *Nat. Rev. Mater.* **2020**, *5*, 5–19. [CrossRef]
11. Wu, X.; Huang, B.; Wang, Q.; Wang, Y. Wide potential and high energy density for an hybrid aqueous supercapacitor. *J. Mater. Chem. A* **2019**, *7*, 19017–19025. [CrossRef]
12. Kulkarni, P.; Nataraj, S.; Balakrishna, R.G.; Nagaraju, D.; Reddy, M. Nanostructured binary and ternary metal sulfides: Synthesis methods and their application in energy conversion and storage devices. *J. Mater. Chem. A* **2017**, *5*, 22040–22094. [CrossRef]
13. Zheng, M.; Xiao, X.; Li, L.; Gu, P.; Dai, X.; Tang, H.; Hu, Q.; Xue, H.; Pang, H. Hierarchically nanostructured transition metal oxides for supercapacitors. *Sci. China Mater.* **2018**, *61*, 185–209. [CrossRef]
14. Karthikeyan, K.; Kalpana, D.; Renganathan, N. Synthesis and characterization of $ZnCo_2O_4$ nanomaterial for symmetric supercapacitor applications. *Ionics* **2009**, *15*, 107–110. [CrossRef]
15. Sankar, K.V.; Selvan, R.K. Fabrication of flexible fiber supercapacitor using covalently grafted $CoFe_2O_4$/reduced graphene oxide/polyaniline and its electrochemical performances. *Electrochim. Acta* **2016**, *213*, 469–481. [CrossRef]
16. Prasankumar, T.; Vigneshwaran, J.; Bagavathi, M.; Jose, S. Expeditious and eco−friendly synthesis of spinel $LiMn_2O_4$ and its potential for fabrication of supercapacitors. *J. Alloy. Compd.* **2020**, *834*, 155060. [CrossRef]
17. Annamalai, K.; Tao, Y.-S. A hierarchically porous CuCo2S4/graphene composite as an electrode material for supercapacitors. *New Carbon Mater.* **2016**, *31*, 336–342.
18. Hu, W.; Chen, R.; Xie, W.; Zou, L.; Qin, N.; Bao, D. $CoNi_2S_4$ nanosheet arrays supported on nickel foams with ultrahigh capacitance for aqueous hybrid supercapacitor applications. *ACS Appl. Mater. Interfaces* **2014**, *6*, 19318–19326. [CrossRef]
19. Liu, Y.; Jiang, G.; Huang, Z.; Lu, Q.; Yu, B.; Evariste, U.; Ma, P. Decoration of hollow mesoporous carbon spheres by NiCo2S4 nanoparticles as electrode materials for hybrid supercapacitors. *ACS Appl. Energy Mater.* **2019**, *2*, 8079–8089. [CrossRef]
20. Wu, Z.; Pu, X.; Ji, X.; Zhu, Y.; Jing, M.; Chen, Q.; Jiao, F. High energy density hybrid supercapacitors from mesoporous NiCo2S4 nanosheets. *Electrochim. Acta* **2015**, *174*, 238–245. [CrossRef]
21. Cai, D.; Wang, D.; Wang, C.; Liu, B.; Wang, L.; Liu, Y.; Li, Q.; Wang, T. Construction of desirable $NiCo_2S_4$ nanotube arrays on nickel foam substrate for pseudocapacitors with enhanced performance. *Electrochim. Acta* **2015**, *151*, 35–41. [CrossRef]
22. Huang, Y.; Shi, T.; Jiang, S.; Cheng, S.; Tao, X.; Zhong, Y.; Liao, G.; Tang, Z. Enhanced cycling stability of $NiCo_2S_4$@ NiO core−shell nanowire arrays for all−solid−state hybrid supercapacitors. *Sci. Rep.* **2016**, *6*, 1–10. [CrossRef]
23. Gao, Y.P.; Huang, K.J. NiCo2S4 materials for supercapacitor applications. *Chem. Asian J.* **2017**, *12*, 1969–1984. [CrossRef]
24. Shen, L.; Wang, J.; Xu, G.; Li, H.; Dou, H.; Zhang, X. $NiCo_2S_4$ nanosheets grown on nitrogen-doped carbon foams as an advanced electrode for supercapacitors. *Adv. Energy Mater.* **2015**, *5*, 1400977. [CrossRef]
25. Guan, B.Y.; Yu, L.; Wang, X.; Song, S.; Lou, X.W. Formation of onion-like $NiCo_2S_4$ particles via sequential ion-exchange for hybrid supercapacitors. *Adv. Mater.* **2017**, *29*, 1605051. [CrossRef]
26. Xia, C.; Li, P.; Gandi, A.N.; Schwingenschlögl, U.; Alshareef, H.N. Is $NiCo_2S_4$ really a semiconductor? *Chem. Mater.* **2015**, *27*, 6482–6485. [CrossRef]
27. Lu, F.; Zhou, M.; Li, W.; Weng, Q.; Li, C.; Xue, Y.; Jiang, X.; Zeng, X.; Bando, Y.; Golberg, D. Engineering sulfur vacancies and impurities in NiCo2S4 nanostructures toward optimal supercapacitive performance. *Nano Energy* **2016**, *26*, 313–323. [CrossRef]
28. Yang, J.; Ma, M.; Sun, C.; Zhang, Y.; Huang, W.; Dong, X. Hybrid $NiCo_2S_4$@MnO_2 heterostructures for high−performance supercapacitor electrodes. *J. Mater. Chem. A* **2015**, *3*, 1258–1264. [CrossRef]
29. Chang, W.-S.; Wu, C.-C.; Jeng, M.-S.; Cheng, K.-W.; Huang, C.-M.; Lee, T.-C. Ternary Ag–In–S polycrystalline films deposited using chemical bath deposition for photoelectrochemical applications. *Mater. Chem. Phys.* **2010**, *120*, 307–312. [CrossRef]
30. Fic, K.; Meller, M.; Menzel, J.; Frackowiak, E. Around the thermodynamic limitations of supercapacitors operating in aqueous electrolytes. *Electrochim. Acta* **2016**, *206*, 496–503. [CrossRef]
31. Zhao, C.; Zheng, W. A review for aqueous electrochemical supercapacitors. *Front. Energy Res.* **2015**, *3*, 23. [CrossRef]
32. Pérez−Madrigal, M.M.; Edo, M.G.; Alemán, C. Powering the future: Application of cellulose−based materials for supercapacitors. *Green Chem.* **2016**, *18*, 5930–5956. [CrossRef]
33. Suganya, N.; Jaisankar, V.; Sivakumar, E. Conducting polymeric hydrogel electrolyte based on carboxymethylcellulose and polyacrylamide/polyaniline for supercapacitor applications. *Int. J. Nanosci.* **2018**, *17*, 1760003. [CrossRef]
34. Timperman, L.; Béguin, F.; Frackowiak, E.; Anouti, M. Comparative study of two protic ionic liquids as electrolyte for electrical double−layer capacitors. *J. Electrochem. Soc.* **2013**, *161*, A228. [CrossRef]
35. Zhong, C.; Deng, Y.; Hu, W.; Qiao, J.; Zhang, L.; Zhang, J. A review of electrolyte materials and compositions for electrochemical supercapacitors. *Chem. Soc. Rev.* **2015**, *44*, 7484–7539. [CrossRef] [PubMed]
36. Erusappan, E.; Pan, G.-T.; Chung, H.-Y.; Chong, S.; Thiripuranthagan, S.; Yang, T.C.-K.; Huang, C.-M. Hierarchical nickel–cobalt oxide and glucose−based carbon electrodes for hybrid supercapacitor with high energy density. *J. Taiwan Inst. Chem. Eng.* **2020**, *112*, 330–336. [CrossRef]
37. Yadav, A.A. Influence of electrode mass−loading on the properties of spray deposited Mn_3O_4 thin films for electrochemical supercapacitors. *Thin Solid Film.* **2016**, *608*, 88–96. [CrossRef]
38. Böckenfeld, N.; Jeong, S.; Winter, M.; Passerini, S.; Balducci, A. Natural, cheap and environmentally friendly binder for supercapacitors. *J. Power Sources* **2013**, *221*, 14–20. [CrossRef]
39. Tsai, Y.-C.; Yang, W.-D.; Lee, K.-C.; Huang, C.-M. An effective electrodeposition mode for porous MnO_2/Ni foam composite for hybrid supercapacitors. *Materials* **2016**, *9*, 246. [CrossRef] [PubMed]

40. Li, D.; Gong, Y.; Pan, C. Facile synthesis of hybrid CNTs/NiCo 2 S 4 composite for high performance supercapacitors. *Sci. Rep.* **2016**, *6*, 1–7.
41. He, X.; Liu, Q.; Liu, J.; Li, R.; Zhang, H.; Chen, R.; Wang, J. High−performance all−solid−state hybridal supercapacitors based on petal−like $NiCo_2S_4$/Polyaniline nanosheets. *Chem. Eng. J.* **2017**, *325*, 134–143. [CrossRef]
42. Zhao, F.; Huang, W.; Shi, Q.; Zhou, D.; Zhao, L.; Zhang, H. Low temperature fabrication of hydrangea−like NiCo2S4 as electrode materials for high performance supercapacitors. *Mater. Lett.* **2017**, *186*, 206–209. [CrossRef]
43. Chen, Y.-Y.; Dhaiveegan, P.; Michalska, M.; Lin, J.-Y. Morphology−controlled synthesis of nanosphere−like NiCo2S4 as cathode materials for high−rate hybrid supercapacitors. *Electrochim. Acta* **2018**, *274*, 208–216. [CrossRef]
44. Gervas, C.; Khan, M.D.; Zhang, C.; Zhao, C.; Gupta, R.K.; Carleschi, E.; Doyle, B.P.; Revaprasadu, N. Effect of cationic disorder on the energy generation and energy storage applications of $NixCo_3-xS_4$ thiospinel. *RSC Adv.* **2018**, *8*, 24049–24058. [CrossRef]
45. Chang, X.; Li, W.; Liu, Y.; He, M.; Zheng, X.; Bai, J.; Ren, Z. Hierarchical $NiCo_2S_4$@ NiCoP core−shell nanocolumn arrays on nickel foam as a binder−free supercapacitor electrode with enhanced electrochemical performance. *J. Colloid Interface Sci.* **2019**, *538*, 34–44. [CrossRef] [PubMed]
46. Arulepp, M.; Leis, J.; Lätt, M.; Miller, F.; Rumma, K.; Lust, E.; Burke, A. The advanced carbide−derived carbon based supercapacitor. *J. Power Sources* **2006**, *162*, 1460–1466. [CrossRef]
47. Mei, B.-A.; Munteshari, O.; Lau, J.; Dunn, B.; Pilon, L. Physical interpretations of Nyquist plots for EDLC electrodes and devices. *J. Phys. Chem. C* **2018**, *122*, 194–206. [CrossRef]
48. Ismail, M.M.; Hemaanandhan, S.; Mani, D.; Arivanandhan, M.; Anbalagan, G.; Jayavel, R. Facile preparation of Mn_3O_4/rGO hybrid nanocomposite by sol–gel in situ reduction method with enhanced energy storage performance for supercapacitor applications. *J. Sol−Gel Sci. Technol.* **2020**, *93*, 703–713. [CrossRef]
49. Saravanan, T.; Anandan, P.; Shanmugam, M.; Azhagurajan, M.; Mohamed Ismail, M.; Arivanandhan, M.; Hayakawa, Y.; Jayavel, R. Facile synthesis of Yb_2O_3–graphene nanocomposites for enhanced energy and environmental applications. *Polym. Bull.* **2020**, *77*, 3891–3906. [CrossRef]
50. Mei, B.-A.; Lau, J.; Lin, T.; Tolbert, S.H.; Dunn, B.S.; Pilon, L. Physical interpretations of electrochemical impedance spectroscopy of redox active electrodes for electrical energy storage. *J. Phys. Chem. C* **2018**, *122*, 24499–24511. [CrossRef]
51. Pan, G.-T.; Chong, S.; Yang, T.C.-K.; Huang, C.-M. Electrodeposited porous $Mn_{1.5}Co_{1.5}O_4$/Ni composite electrodes for high−voltage hybrid supercapacitors. *Materials* **2017**, *10*, 370. [CrossRef]
52. Fan, Y.-M.; Liu, Y.; Liu, X.; Liu, Y.; Fan, L.-Z. Hierarchical porous NiCo2S4−rGO composites for high−performance supercapacitors. *Electrochim. Acta* **2017**, *249*, 1–8. [CrossRef]
53. Hou, L.; Bao, R.; Chen, Z.; Rehan, M.; Tong, L.; Pang, G.; Yuan, C. Comparative investigation of hollow mesoporous $NiCo_2S_4$ ellipsoids with enhanced pseudo−capacitances towards high−performance hybrid supercapacitors. *Electrochim. Acta* **2016**, *214*, 76–84. [CrossRef]
54. Prabaharan, S.; Vimala, R.; Zainal, Z. Nanostructured mesoporous carbon as electrodes for supercapacitors. *J. Power Sources* **2006**, *161*, 730–736. [CrossRef]
55. Huang, Y.; Cheng, M.; Xiang, Z.; Cui, Y. Facile synthesis of $NiCo_2S_4$/CNTs nanocomposites for high−performance supercapacitors. *R. Soc. Open Sci.* **2018**, *5*, 180953. [CrossRef]
56. Zhang, M.; Liu, H.; Song, Z.; Ma, T.; Xie, J. Self−assembling $NiCo_2S_4$ nanorods arrays and T−Nb_2O_5 nanosheets/three−dimensional nitrogen−doped garphene hybrid nanoarchitectures for advanced hybrid supercapacitor. *Chem. Eng. J.* **2020**, *392*, 123669. [CrossRef]
57. Gao, Y.; Wu, B.; Hei, J.; Gao, D.; Xu, X.; Wei, Z.; Wu, H. Self−assembled synthesis of waxberry−like open hollow $NiCo_2S_4$ with enhanced capacitance for high−performance hybrid asymmetric supercapacitors. *Electrochimica Acta* **2020**, *347*, 136314. [CrossRef]
58. Li, R.; Wang, S.; Huang, Z.; Lu, F.; He, T. $NiCo_2S_4$@$Co(OH)_2$ core−shell nanotube arrays in situ grown on Ni foam for high performances hybrid supercapacitors. *J. Power Sources* **2016**, *312*, 156–164. [CrossRef]
59. Zhao, Y.; He, X.; Chen, R.; Liu, Q.; Liu, J.; Song, D.; Zhang, H.; Dong, H.; Li, R.; Zhang, M. Hierarchical $NiCo_2S_4$@ $CoMoO_4$ core−shell heterostructures nanowire arrays as advanced electrodes for flexible all−solid−state hybrid supercapacitors. *Appl. Surf. Sci.* **2018**, *453*, 73–82. [CrossRef]
60. Zhang, L.; Wang, W.; Cheng, J.; Shi, Y.; Zhang, Q.; Dou, P.; Xu, X. Skeleton networks of graphene wrapped double−layered polypyrrole/polyaniline nanotubes for supercapacitor applications. *J. Mater. Sci.* **2018**, *53*, 787–798. [CrossRef]
61. Lu, X.; Liu, T.; Zhai, T.; Wang, G.; Yu, M.; Xie, S.; Ling, Y.; Liang, C.; Tong, Y.; Li, Y. Improving the cycling stability of metal–nitride supercapacitor electrodes with a thin carbon shell. *Adv. Energy Mater.* **2014**, *4*, 1300994. [CrossRef]
62. Ismail, M.M.; Vigneshwaran, J.; Arunbalaji, S.; Mani, D.; Arivanandhan, M.; Jose, S.P.; Jayavel, R. Antimonene nanosheets with enhanced electrochemical performance for energy storage applications. *Dalton Trans.* **2020**, *49*, 13717–13725. [CrossRef] [PubMed]